**Atmospheric
Chemistry
and Physics
Discussions**

# Spectral optical properties of long-range transport Asian dust and pollution aerosols over Northeast Asia in 2007 and 2008

J. Jung[1],[*], Y. J. Kim[1], K. Y. Lee[1], M. G.-Cayetano[1], T. Batmunkh[1], J.-H. Koo[2],[**], and J. Kim[2]

[1]Advanced Environmental Monitoring Research Center (ADEMRC), Gwangju Institute of Science and Technology (GIST), Gwangju 500-712, Korea
[2]Department of Atmospheric Science, Yonsei University, Seoul 120-749, Korea
[*]now at: Institute of Low Temperature Science, Hokkaido University, Sapporo 060-0819, Japan
[**]now at: School of Earth and Atmospheric Sciences, Georgia Institute of Technology, Atlanta, USA

---

**Spectral aerosol optical properties**

J. Jung et al.

Printer-friendly Version

Interactive Discussion

## Abstract

As a part of the IGAC (International Global Atmospheric Chemistry) Mega-cities program, aerosol physical and optical properties were continuously measured from March 2007 to March 2008 at an urban site (37.57° N, 126.94° E) in Seoul, Korea. Spectral optical properties of long-range transported Asian dust and pollution aerosols have been investigated based on the year long measurement data. Optically measured black carbon/thermally measured elemental carbon (BC/EC) ratio showed clear monthly variation with high values in summer and low values in winter mainly due to the enhancement of light attenuation by the internal mixing of EC. Novel approach has been suggested to retrieve the spectral light absorption coefficient ($b_{abs}$) from Aethalometer raw data by using BC/EC ratio. Mass absorption efficiency, $\sigma_{abs}$ ($=b_{abs}$/EC) at 550 nm at the measurement site was determined to be 9.0±1.3, 8.9±1.5, 9.5±2.0, and 10.3±1.7 $m^2\,g^{-1}$ in spring, summer, fall, and winter, respectively with an annual mean of 9.4±1.8 $m^2\,g^{-1}$. Threshold values to classify severe haze events were suggested in this study. Increasing trend of aerosol single scattering albedo (SSA) with wavelength was observed during Asian dust events while little spectral dependence of SSA was observed during long-range transport pollution (LTP) events. Satellite aerosol optical thickness (AOT) and Hysplit air mass backward trajectory analyses as well as chemical analysis were performed to characterize the dependence of spectral optical properties on aerosol type. Results from this study can provide useful information for studies on regional air quality and aerosol's effects on climate change.

## 1  Introduction

Radiative forcing (RF) is defined as "the change in net (down minus up) irradiance (solar plus long wave; in $W\,m^{-2}$) at the tropopause after allowing for stratospheric temperatures to readjust to radiative equilibrium, but with surface and tropospheric temperatures and state held fixed at the unperturbed values" (Ramaswamy et al., 2001). The

aerosol RF depends on not only their spatial distributions, but also the size, shape, and chemical composition of the particles. The aerosol RF influences on various aspects (e.g., cloud formation) of the hydrological cycles. The total direct aerosol RF, derived from models and observations, is estimated to be $-0.5\pm0.4\,\mathrm{W\,m^{-2}}$, with a medium-low level of scientific understanding. The estimates are: $-0.4\pm0.2\,\mathrm{W\,m^{-2}}$ (sulfate), $-0.05\pm0.05\,\mathrm{W\,m^{-2}}$ (fossil fuel organic carbon), $+0.2\pm0.15\,\mathrm{W\,m^{-2}}$ (fossil fuel black carbon), $+0.03\pm0.12\,\mathrm{W\,m^{-2}}$ (biomass burning), $-0.1\pm0.1\,\mathrm{W\,m^{-2}}$ (nitrate) and $-0.1\pm0.2\,\mathrm{W\,m^{-2}}$ (mineral dust) (IPCC, 2007). However, there is substantial uncertainty in the magnitude and spatial distribution of the RF by aerosols. One of the largest sources of uncertainty in estimation of the aerosol RF is the Asian aerosol. A mixture of both heavy air pollution over the Asian continent and seasonal increases of desert dust particles results in very complex optical properties of the particles (Höller et al., 2003). An expected tripling of Asian emissions from 1985 to 2010 implies that aerosols and aerosol precursor emissions will increase sharply over the next decade, which makes regular observations an urgent necessity (Jacob et al., 1999).

Radiative transfer models used to predict the aerosol RF are based on spectral optical properties calculated by Mie-Theory. While this is a reasonable approach for spherical particles like aqueous sulfate aerosol, soot particles possess a rather complex fractal-like morphology which makes a reliable modeling of their optical properties much more difficult. Moreover, the mixing state of EC in the atmospheric aerosol is usually assumed to be external, which overestimates the above net cooling effect significantly (Jacobson, 2001). Climate models typically treat EC as the only light-absorbing aerosol compounds. If spectral dependence of aerosol light absorption is underestimated in models, the aerosol positive RF will be understated (Bond, 2001). So characterization of additional aerosol absorption at short wavelength is very important for the better estimation of the aerosol RF. Heintzenberg et al. (1997) pointed out the importance of the single-scattering albedo in climate models and the essential role of accurate observational data. Concerning the wavelength dependence of the single-scattering albedo data are still very scarce (Dubovik et al., 2002; Höller et al.,

2003). Spectral characteristics of aerosol light absorption and scattering are not well characterized in part due to the lack of long-term in-situ measurement over Northeast Asia.

The objective of this research is to characterize the spectral optical properties of long-range transport Asian Dust and pollution aerosols as well as urban aerosols. Seasonal pattern of spectral optical properties of urban aerosols in the measurement site has been investigated. The source regions and transport pathway of anthropogenic pollution and Asian dust have been characterized based on a satellite aerosol optical thickness (AOT) and back-trajectory analysis.

## 2  Measurement and method

As a part of the IGAC Mega-cities program, aerosol physical and optical properties were continuously measured from March 2007 to March 2008 at an urban site (37.57° N, 126.94° E) in Seoul, Korea (Fig. 1). Seoul has population more than 10.4 million with over 2.8 million automobiles. All instruments were was installed in a temperature controlled trailer at the rooftop of the Science Building (∼30 m height) of Yonsei University, which is located in the north-west part of Seoul. Sample air was aspirated from the rooftop of the trailer to each instrument. The time represents the Korean local time (GMT+09:00) unless otherwise noted. An overview of the instrumentation is given in Table 1. All parameters in Table 1 were hourly averaged and used in this study.

### 2.1  Sunset semi-continuous OC/EC analyzer

Particulate carbonaceous aerosol was measured using a Sunset Laboratory semi-continuous OC/EC analyzer (Sunset Lab, Model RT3015) with thermal-optical transmittance (TOT) protocol for pyrolysis correction (Birch and Cary, 1996; Jeong et al., 2004; Kim et al., 2006). For the analysis of OC and EC, ambient air was drawn at

8 l/min (LPM) through a $PM_{2.5}$ sharp-cup cyclone. The sampled aerosol was passed through a multi-channel parallel-plate denuder with carbon-impregnated-filter (CIF) before it was collected on a quartz-fiber filter in order to remove semi-volatile organic vapors that could be potentially absorbed onto the quartz-filter media (Turpin et al., 2000). The OC and EC were analyzed based on NIOSH (National Institute for Occupational Safety and Health) 5040 method temperature profile. The analyzer was automatically calibrated at the end of every analysis cycle by injecting an internal-standard $CH_4$ mixture (5% $CH_4$ in He), via a fixed injection-volume loop, to compensate for the variability in the instrument's non-dispersive infrared (NDIR) sensor responses. For temporal resolution of 1 h (44 min of collection) measurement, the detection limit of EC was determined to be 0.01 $\mu g\,C\,m^{-3}$, calculated as three times the standard deviation ($3\sigma$) of filtered air measurement (dynamic blank). The uncertainty of this system was reported to be 5% (Polidori et al., 2006).

## 2.2 7-wavelength Aethalometer

The 7-$\lambda$ Aethalometer (Magee Scientific, Model AE31) measures the optical attenuation (absorbance) of light from LED lamps emitting at seven wavelengths (370, 470, 520, 590, 660, 880, and 950 nm) with a typical half-width of 20 nm (Hansen, 2005). The black carbon (BC) determination assumes that all the light-absorbing materials are composed of BC. The specific mass attenuation efficiency, $\sigma_{ATN}$ of the aethalometer used for the determination of the BC concentration was 14 625/$\lambda [m^2\,g^{-1}]$ as recommended by the manufacturer. The flow rate was maintained at 4 LPM corresponding to a 2.5 $\mu m$ cut-point of $PM_{2.5}$ cyclone (BGI inc., SCC1.829). As shown in Table 2, detection limit of the aethalometer BC was determined to be 0.16–0.28 $\mu g\,m^{-3}$ with a flow rate of 4 LPM and 5-min time interval, calculated as three times the standard deviation ($3\sigma$) of the dynamic blank. Uncertainty of the aethalometer reported by the manufacturer is ±5% (Hansen, 2005). Details of the instrument can be found elsewhere (Hansen et al., 2005; Schmid et al., 2006; Weingartner et al., 2003). To account for the

"shadowing" effect due to filter loading (decrease in aethalometer sensitivity), $R(\text{ATN})$, the loading correction was done as suggested by Weingartner et al. (2003). Even though humidity effect on the aethalometer BC measurement was negligible (Schmid et al., 2006), the aerosol was dried to RH<40% by a diffusion dryer prior to particle detection.

## 2.3 Nephelometer

Light scattering coefficient, $b_{\text{scat}}$ at 550 nm of ambient particles in the total suspended particle regime was measured by an ambient nephelometer (OPTEC, Model NGN2) with an open air inlet. Periodic ZERO (Rayleigh clean air) air and SPAN gas calibrations were performed in order to monitor and correct for instrument gain and zero intercept drift due to temperature changes and/or dirt accumulating on the measurement chamber optics. ZERO air calibration was usually performed more often (every 12 h) than SPAN gas calibration, which was done every week with dense gas such as HFC-134a (Suva 134a). Uncertainty of the ambient nephelometer reported by the manufacturer is ±10% with 2 min time interval (Optec, 1993). For time resolution of 2 min, the detection limit of $b_{\text{scat}}$ was measured to be 4.32 Mm$^{-1}$, calculated as $3\sigma$ of dynamic blank.

## 2.4 Aerosol spectrometer

PM$_{10}$/PM$_{2.5}$/PM$_{1.0}$ mass concentrations and particle number size distribution in the range of 0.25-32 μm were measured by an aerosol spectrometer system (Grimm Labortechnik Ltd., Model 265). The aerosol spectrometer system consists of an aerosol spectrometer (Grimm Labortechnik Ltd., Model 1.108) and a dry air dilution system combined with a heated sampling system. Ambient air is drawn into the instrument via an internal volume-controlled pump at a rate of 1.2 LPM. Each sampled single particle is illuminated by a 675-nm laser beam and each scattering signal is detected by a photo diode. In accordance with the Mie theory each measured scatter pulse height

is classified in each size bin (32 channels). Particle mass distribution is obtained from volume distribution calculated from particle number distribution and a density factor corresponding to the GRIMM established "urban environment" factor (Grimm, 2002; Grimm and Eatough, 2009). According to the manufacturer, the reproducibility of the aerosol spectrometer in particle counting is ±2%. Raw particle number and mass concentration were measured every minute under dry condition (RH<40%) by diluting the sample air with dry clean air. Based on automatically controlled inlet heating system with 110°C heating for 15 min and no heating for 15 min, the number concentrations of ambient and refractive aerosols was measured every minute. Finally the number concentration of volatile aerosol was determined from the difference between hourly average ambient and refractive number concentrations with 1-h time interval. The detection limit and uncertainties of the measurement systems are summarized in Table 2.

## 2.5  Skyradiometer

Aerosol optical thickness (AOT) was determined for every 10 min time interval based on the Skyradiometer (PREDE, Model POM-2) data measured at 11 channels (315, 340, 380, 400, 500, 675, 870, 940, 1020, 1600, and 2200 nm). Skyradiometer has two observation geometries, which are principal method and almucantar method. One geometric situation of common use is making measurements in the principal plane, that is, pointing along a plane with the same azimuth angle of the Sun, and letting zenith angle $\theta$ vary. The other observation geometry consists of carrying out measurements in the solar almucantar, that is, pointing from the measurements' place along a conical surface with the same zenith angle $\theta_0$ of the Sun, and letting azimuth angle $\Phi$ vary. This study conducted vertical and horizontal measurements sequentially in each cycle based on the principal and almucantar methods, respectively, for 10-min time interval. The software code SKYRAD.pack (Nakajima et al., 1996) was used to retrieve AOT from data of direct and diffuse solar radiation. Only cloud-screened and quality-assured data were used in this study.

## 3   Analytical method

It is well-known that light attenuation coefficient, $b_{ATN}$ is generally larger than light absorption coefficient, $b_{abs}$ due to optical interactions of the filter substrate with the deposited aerosol (Petzold et al., 1997; Kopp et al., 1999; Ballach et al., 2001; Wein-gartner et al., 2003; Arnott et al., 2005). The most significant filter-particle interactions and the resulting biases are: 1) multiple scattering of light by the filter fibers enhances the optical path length, resulting in positive bias on $b_{ATN}$, 2) enhanced absorption of scattered light with increasing filter loading reduces the optical path length, so called "shadowing effect", which reduces $b_{ATN}$, and 3) the filter reflectance (scattering in back-wards hemisphere) and hence the measured attenuation depends on the optical prop-erties of the deposited particles (bias in $b_{ATN}$ depends on physico-chemical properties of the particles).

Because previous studies have already discussed in detail about the retrieval of $b_{abs}$ from Aethalometer $b_{ATN}$ (Weingartner et al., 2003; Arnott et al., 2005; Schmid et al., 2006), only brief description is given here.

Aerosol light absorption coefficient, $b_{abs}$ determined by the Aethalometer can be expressed as (Weingartner et al., 2003)

$$b_{abs} = \frac{b_{ATN}}{C \cdot R(ATN)} \tag{1}$$

where the constant factor $C (\geq 1)$ corrects for multiple light scattering effects within the filter and $R(ATN)$ ($\leq 1$) accounts for the "shadowing" effect due to filter loading (de-crease in Aethalometer sensitivity). The attenuation, ATN (=100·ln($I_0/I$)) is typically given as percentage value and is defined by the relationship between the light inten-sities transmitted through the particle-laden ($I$) and a blank spot of the filter ($I_0$). The loading correction can be expressed as (Weingarter et al., 2003)

$$R(ATN) = \left(\frac{1}{f} - 1\right) \cdot \frac{\ln ATN - \ln 10}{\ln 50 - \ln 10} + 1 \tag{2}$$

where the shadowing factor, $f$ is a parameter that depends on the type of aerosol and

ATN. The $f$ can be estimated as

$$f = a(1 - \omega_0) + 1 \qquad (3)$$

where $a$=0.87±0.10 and 0.85±0.05 at $\lambda$=450 and 660 nm, respectively (Weingartner et al., 2003).

5    For the determination of the multiple scattering correction factor, $C$, aerosol scattering is non-negligible (Arnott et al., 2005). Overall correction factor, $C$ can be expressed as

$$C = C^* + m_s \frac{\omega_0}{1 - \omega_0} \qquad (4)$$

where $C^*$ represents the multiple scattering correction factor corrected for aerosol scat-

10  tering. $m_s$ and $\omega_0$ represent aerosol scattering correction factor and single scattering albedo, respectively (Arnott et al., 2005). The dependence of $C$ on $\lambda$ can be expressed by the coefficients $A$ and $B$, which depends on Ångström exponent of aerosol absorption, $\alpha_a$ (Schmid et al., 2006).

$$C(\lambda) = C_{ref} \cdot \frac{\lambda^{A\ln(\lambda/nm)+B}}{\lambda_{ref}^{A\ln(\lambda/nm)+B}} \qquad (5)$$

15  $\alpha_a$ was determined by the following iterative procedure: i) use $\alpha_{ATN}$ (from Aethalometer data) as a first approximation for $\alpha_a$, ii) calculate $b_{abs}$, iii) derive a refined $\alpha_a$ value based on $b_{abs}$ and iv) repeat steps ii) and iii) until $b_{abs}$ converges.

Spectral dependence of $b_{abs}$ was easily characterized by Ångström exponent for absorption, $\alpha_a$.

20  $$b_{abs}(\lambda) = A \cdot \lambda^{\alpha_a} \qquad (6)$$

$\alpha_a$ is estimated by transformation of Eq. (6) to a linear form,

$$\ln(b_{abs}(\lambda)) = \ln(A) + \alpha_a \cdot \ln(\lambda) \qquad (7)$$

Applying the least square fitting $\alpha_a$ is taken from the slope of $b_{abs}$ against wavelength, $\lambda$. In this study, $\alpha_a$ (UV–blue) is defined as the Ångström exponent for absorption in the wavelength range between 370 and 520 nm while $\alpha_a$ (VIS) is between 520 and 880 nm.

The NOAA/ARL HYSPLIT (HYbrid Single-Particle Lagrangian Trajectory) air mass backward trajectory analysis (Draxler and Rolph, 2003; Rolph, 2003) and Moderate Resolution Imaging Spectro-radiometer (MODIS) satellite image analysis were used to characterize potential source regions and the transport pathway of the air mass. Air mass backward trajectories ended at the measurement site were computed for 200, 500, and 1000 m above ground level (AGL) heights using the HYSPLIT model. The National Weather Service's National Centers for Environmental Prediction (NCEP) runs a series of computer analyses and forecasts operationally. One of the operational systems is the GDAS (Global Data Assimilation System). The GDAS is run 4 times a day, ie, at 00:00, 06:00, 12:00, and 18:00 UTC. The 3-hourly archive data come from NCEP's GDAS were used for the trajectory calculation. Up to 20% errors of the traveled distance are typical for those trajectories computed from analyzed wind field (Stohl, 1998). Thus, calculated air mass pathways indicate the general airflow pattern rather than the exact pathway of an air mass. All back-trajectories were calculated at 02:00 UTC and 05:00 UTC (11:00 LT and 14:00 LT, respectively) extending to 96 h backward with 1-h time interval. Aerosol optical thickness (AOT) data retrieved by the new V5.2 version of the NASA MODIS algorithm, called Collection 005 (C005) (Levy et al., 2007a, b) were used in this study. AOT data which is part of the MODIS Terra/Aqua Level-2 gridded atmospheric data product are available on the MODIS web site http://modis.gsfc.nasa.gov/.

## 4  Result and discussion

### 4.1  Retrieval of spectral absorption coefficient of atmospheric aerosol

To retrieve $b_{abs}$ from aethalometer $b_{ATN}$, it is essential to determine the multiple scattering correction factor, $C^*$ accurately which varies depending on the mixing state of EC. Since it is difficult to determine the mixing state of EC in the atmosphere, internal or external mixture of EC was assumed in the most of models and field studies (Hasegawa and Ohta, 2002; Naoe and Okada, 2001; Posfai et al., 1999). Previous calibration studies involving $C^*$ of different mixing states of EC are summarized in Table 3. It was reported that $C^*$ was determined to be 1.8–2.2 and 3.6–4.55 for the external mixture and the internal mixture of EC, respectively (Arnott et al., 2005; Schmid et al., 2006; Weingartner et al., 2003).  Figure 2 shows monthly variation of BC/EC ratio based on optically measured BC and thermally measured EC by the aethalometer and the semi-continuous Sunset OC/EC analyzer, respectively.  Because the aethalometer BC is obtained from the optical attenuation of light by EC deposited on a filter, the magnitude of BC is highly influenced by additional absorption by light absorbing aerosols such as dust particles and organic aerosol as well as the mixing state of EC. Petzold et al. (1997) argued that, for internal mixtures of EC and some mainly scattering material, an aethalometer response may be enhanced by up to a factor of 2 (for EC contents of about 3%), compared to external mixtures.  Weingartner et al. (2003) also observed that spectral absorption (370–950 nm) of an aethalmeter was enhanced by up to a factor of 1.5 for soot coated with organic aerosol, compared to externally mixed soot with ammonium sulfate. They also found that almost no enhancement of an aethalometer absorption at 880 nm was observed for externally mixed soot with ammonium sulfate relative to reference soot. Since this study uses BC measured at 880 nm where only EC is absorbing aerosol, the change in measured BC value is mainly due to change of mixing state of EC. In contrary, thermally measured EC is independent of the mixing state of EC. As seen in Fig. 2, BC/EC ratio shows clear monthly variation with higher values in summer and lower values in winter. The enhanced BC concentration in

summer is mainly due to the increase of absorption capacity of EC through the internal mixing (or coating) with organic and inorganic aerosols. Snyder and Schauer (2007) also reported the enhancement of light absorption capacity of EC through the coating with secondary organics. So, in this study BC/EC ratio was used as an indicator of the mixing state of EC.

This study determined $C^*$ based on BC/EC ratio, assuming most of EC in summer (highest BC/EC ratio) is internal mixture while that in winter is external mixture (lowest BC/EC ratio). $C^*$ of 2.1 and 4.0 was used in this study for externally and internally mixture of EC, respectively suggested by Schmid et al (2006). Retrieval of $C^*$ based on BC/EC ratio is shown in Fig. 3. During the measurement period, monthly average BC/EC ratio varies from 0.90±0.09 to 1.37±0.18. Regression equation of $C^*$ versus BC/EC ratio was obtained as followed;

$$C^* = 4.05 \cdot \frac{BC}{EC} - 1.55 \qquad (8)$$

$C^*$ at each wavelength and $\alpha_a$(370–950 nm) between 370 and 950 nm were obtained based on Eqs. (1)–(8) and shown in Fig. 4. $\alpha_a$(370–950 nm) shows clear monthly variation with lower values (1.33–1.39) in summer and higher values (1.58–1.65) in winter. This seasonal trend can be partially explained by seasonal trend of particulate PAHs which is one of the major strong UV absorbing components. Previous study reported clear seasonal trend of PAHs with higher values in winter of Seoul, Korea during 1998–1999 (Park et al., 2002). Particulate PAHs in PM$_{2.5}$ in winter were almost 8 times higher than those in summer. Seasonal variations of PAH concentration is generally attributed to increased emissions during the cold season, principally fossil fuel combustion for space heating purposes. Other factors known to contribute to higher wintertime PAHs concentrations include lower atmospheric mixing heights, lower temperatures, and decreased photochemical oxidation (Park et al., 2002).

Site specific mass attenuation efficiency, $\sigma_{ATN}(=b_{ATN}/EC)$ was determined based on thermally measured EC and the aethalometer raw $b_{ATN}$ data. Mass absorption efficiency, $\sigma_{abs}(=b_{abs}/EC)$ was determined based on thermally measured EC and $b_{abs}$.

**ACPD**

10, 2397–2444, 2010

**Spectral aerosol optical properties**

J. Jung et al.

Title Page

| Abstract | Introduction |
| Conclusions | References |
| Tables | Figures |

◄ | ►►

◄ | ►

Back | Close

Full Screen / Esc

Printer-friendly Version

Interactive Discussion

Figure 5 shows seasonal variations of spectral $\sigma_{ATN}$ and $\sigma_{abs}$. Magee BC in Fig. 5 represents $\sigma_{ATN}$ widely used in BC calculation from AE31 aethalometer. It was found that the AE31 aethalometer underestimated BC by 20% in winter than thermally measured EC while it overestimated 20, 40, and 10% in spring, summer, and fall, respectively. $\sigma_{abs}$ at 550 nm wavelength was obtained to be 9.0±1.3, 8.9±1.5, 9.5±2.0, and 10.3±1.7 m$^2$ g$^{-1}$ in spring, summer, fall, and winter, respectively. Annual mean $\sigma_{abs}$ of 9.4±1.8 m$^2$ g$^{-1}$ at the measurement site was slightly lower than that of 10.5±0.7 m$^2$ g$^{-1}$ observed at six different locations in Asia (Japan, Korea, China, and Thailand) (Kondo et al., 2009).

## 4.2 Retrieval of spectral scattering coefficient of atmospheric aerosol

Since the nephelometer used in this study only measures $b_{scat}$ at 550 nm, spectral $b_{scat}$ was retrieved based on $b_{scat}$ at 550 nm and spectral dependence of $b_{scat}$. First, light extinction coefficient, $b_{ext}$ at 550 nm was obtained from the sum of $b_{scat}$ and $b_{abs}$ at 550 nm. And then $b_{ext}$ at each wavelength was retrieved based on Ångström exponent of aerosol light extinction, $\alpha_e$ obtained from column integrated AOT measured by the Skyradiometer.

$$b_{ext}(\lambda) = b_{ext}(550\,\text{nm}) \cdot \left(\frac{\lambda}{550\,\text{nm}}\right)^{-\alpha_e} \tag{9}$$

where $\alpha_e$ at UV and visible wavelength regions were obtained from spectral AOT measured by the Skyradiometer as;

$$\alpha_e\_UV = -\frac{\log(AOT(550\,\text{nm})) - \log(AOT(380\,\text{nm}))}{\log(550\,\text{nm}) - \log(380\,\text{nm})} \tag{10}$$

$$\alpha_e\_vis = -\frac{\log(AOT(870\,\text{nm})) - \log(AOT(550\,\text{nm}))}{\log(870\,\text{nm}) - \log(550\,\text{nm})} \tag{11}$$

Finally spectral $b_{scat}$ was obtained from spectral $b_{ext}$ after subtracting spectral $b_{abs}$. Average $\alpha_e\_UV$ was determined to be 1.08, 0.92, 1.15, and 1.05 in spring, summer, fall,

and winter, respectively. Average $\alpha_{e\_vis}$ was 1.17, 1.20, 1.33, and 1.25 in spring, summer, fall, and winter, respectively. Seasonal variations of spectral $b_{abs}$ and $b_{scat}$ as well as $\alpha_a$ and Ångström exponent of $b_{scat}$, $\alpha_s$ from 370 nm to 950 nm are shown in Fig. 6. Highest spectral dependence of $b_{abs}$ was observed in winter as discussed in Fig. 4. Average $b_{abs}$ at 550 nm was determined to be 26.5±13.3, 21.1±12.7, 28.4±21.9, and 34.8± 24.2 Mm$^{-1}$ in spring, summer, fall, and winter, respectively. Highest values are observed in winter mainly due to low boundary layer height and increased emission from low temperature combustion while lowest values are in summer mainly due to clean southerly wind from Pacific Ocean. Average $b_{scat}$ at 550 nm was determined to be 264.6±226.3, 208.5±239.6, 201.4±250.5, and 225.7±247.4 Mm$^{-1}$ in spring, summer, fall, and winter, respectively. Highest $b_{scat}$ in spring was mainly due to frequent transport of pollution and Asian dust aerosols from Asian continent (Kim et al., 2001, 2006; Park and Kim, 2006; Lee et al., 2007; Kim, 2008). $\alpha_s$ was determined to be 1.13, 1.08, 1.24, and 1.12 in spring, summer, fall, and winter, respectively. Since lower $\alpha_s$ indicates larger particle size while higher one does small particle size, highest $\alpha_s$ in fall indicates freshly emitted fine particle dominance such as post-harvest biomass burning (Balis et al., 2003; Lee et al., 2005; Badarinath et al., 2008; Ryu et al., 2006). Because of high RH of 74.7±13.6% in summer, lowest $\alpha_s$ in summer might be due to the increase of particle size through water uptake.

## 4.3  Spectral single scattering albedo of atmospheric aerosol

Single scattering albedo, SSA of ambient aerosol was obtained from the ratio of $b_{scat}$ to $b_{ext}(=b_{scat}+b_{abs})$. Figure 7 shows seasonal variations of spectral SSA. Average SSA at 550 nm was determined to be 0.88±0.07, 0.84±0.10, 0.82±0.09, and 0.84±0.06 in spring, summer, fall, and winter, respectively. Average SSA during the entire measurement period was determined to be 0.85±0.09. It is comparable to 0.86 in Guangzhou (Andreae et al., 2008) but slightly higher than 0.81–0.85 measured at the rural site of Xianghe in China (~70 km southeast of Beijing) (Li et al., 2007) and 0.81 in Beijing

(Bergin et al., 2001). During the entire measurement period, highest $EC/PM_{10}$ ratio was determined to be 7.8±3.8% in fall, followed by summer (7.4±5.8%), winter (6.2±2.5%), and spring (4.6±2.8%). Lowest SSA in fall can be explained by the highest $EC/PM_{10}$ ratio. Even though similar $EC/PM_{10}$ ratios were obtained in spring and summer, higher SSA was determined in summer relative to spring. This was mainly due to the enhancement of $b_{scat}$ under humid condition in summer. Highest SSA in spring can be attributed to the enhancement of $b_{scat}$ by Asian dust and long-range transport pollution aerosols from Asian continent (Kim et al., 2001; Lee et al., 2007).

Ångström exponent of SSA, $\alpha_{SSA}$ in UV (370–520 nm) and visible (590–950 nm) wavelength for different seasons are also shown in Fig. 7. Increasing trend of SSA with wavelength was mainly due to strong spectral dependence of $b_{abs}$. Strongest spectral dependence of SSA was observed in winter with $\alpha_{SSA}$-UV of -0.18. This is mainly due to the increase of additional absorption by UV absorbing compound (PAHs, etc). SSA at 550 nm under relatively dry (RH<60%) and humid (RH>60%) condition are also plotted as a function $PM_{10}$ mass concentration in Fig. 7. Average RH was determined to be 42.7 and 76.6% under the dry and humid conditions, respectively. Each data point in Fig. 7 represents average value with one standard deviation range for each $10\,\mu g\,m^{-3}$ incremental interval for $PM_{10} < 100\,\mu g\,m^{-3}$ and for $30\,\mu g\,m^{-3}$ incremental interval for $PM_{10} > 100\,\mu g\,m^{-3}$. The difference of SSA under the dry and humid conditions (ΔSSA) is also plotted in Fig. 7. SSA for $PM_{10} < 10\,\mu g\,m^{-3}$ decreased down to 0.71±0.12 and 0.72±0.12 under relatively dry and humid conditions, respectively, which reveals that background aerosols are highly absorbing. As $PM_{10}$ mass increases, SSA increases up to 0.90±0.02 and 0.94±0.02 for $PM_{10} < 200\,\mu g\,m^{-3}$ under the dry and humid conditions, respectively. It was found that average SSA under the humid condition is ∼7% higher than that under the dry condition mainly due to the enhancement of aerosol scattering by water uptake. Interestingly as $PM_{10}$ increases $> 100\,\mu g\,m^{-3}$, ΔSSA sharply decreases from ∼0.075 down to ∼0.035. Since high $PM_{10}$ mass concentration $> 150\,\mu g\,m^{-3}$ was observed during the Asian dust periods as summarized in Table 4, decreasing trend of ΔSSA under high aerosol loading

can be explained by increased contribution of hydrophobic dust particles to total $PM_{10}$ mass concentration.

Frequency distributions of SSA at 550 nm are shown in Fig. 8 for four different seasons. Blue triangle and red diamond represent relatively clean ($PM_{10}<50\,\mu g\,m^{-3}$) and polluted ($PM_{10}>100\,\mu g\,m^{-3}$) periods, respectively. Bi-modal distribution of SSA centered at 0.82 (first mode) and 0.94 (second mode) are clearly observed in all season. The mass fraction of carbonaceous aerosols-especially EC to total PM mass concentration was dominantly increased during the clean period in the megacities of Korea (Kim et al., 2007) and China (Jung et al., 2009a, b) while that of secondary aerosols such as sulfate and nitrate were during the polluted period. Those can explain the dominance of SSA in the first mode during the clean periods due to increase of light absorption by EC and that in the second mode during the polluted periods due to increase of light scattering by secondary aerosols. The highest frequency of SSA in spring is observed in the second mode, which can be explained by frequent occurrence of Asian dust and haze events (Kim et al., 2001, 2006; Lee et al., 2007; Kim, 2008). In contrary, the highest frequency of SSA is observed in the first mode in winter, which indicates the increased contribution of light absorbing aerosol in winter. The frequency of SSA in the first mode increases with season change from spring to winter while it decreases in the second mode. Even though average $PM_{10}$ mass concentration was similar between summer and fall, frequency distribution of SSA in the second mode was slightly higher in summer. This is mainly due to high RH in summer which enhances aerosol scattering by water uptake as discussed in Fig. 7.

## 4.4 Characteristics of spectral aerosol optical properties of long-range transport aerosol

Temporal variation of hourly average $PM_{10}$ mass concentration at the measurement site is plotted in Fig. 9. During the measurement period, several severe haze events were observed. These severe haze events were categorized into either long-range transport pollution (LTP) or Asian dust cases based on the analysis results of MODIS

aerosol optical thickness (AOT) and Hysplit air mass back-trajectories. LTP haze and Asian dust events are expressed as red and black circles, respectively, in Fig. 9. Most of Asian dust event occurred in spring except two cases in winter.

### 4.4.1 Asian dust particles

Because Korea is located in the downwind area of Asian continent, dust aerosol particles originated from desert regions in China are frequently transported over Korea mainly in spring (Kim et al., 2001; Park and Kim, 2006; Kim, 2008). MODIS RGB image, AOT, and AOT Ångström exponent on 31 March 2007 are shown in Fig. 10. High aerosol loadings are observed over China with high AOT of >1.0. Asian dust layer is clearly seen over Northern China to Yellow Sea with high AOT of >1.0 and low Ångström exponent of <0.4. During the entire measurement period, Asian dust events were observed five times in spring and twice in winter. Average $PM_{10}$ mass concentration during the Asian dust periods ranged 92.3 µg m$^{-3}$ to 1089.0 µg m$^{-3}$. Severe Asian dust events were observed during 31 March–1 April 2007 (AD2_07) with an average $PM_{10}$ of 544.1±250.6 µg m$^{-3}$. Aerosol physical and optical properties observed during the Asian dust events are summarized in Table 4. MODIS RGB images and Hysplit air mass back-trajectories arriving at the measurement site during the Asian dust periods are shown in Fig. 11. Red, blue, and yellowish green lines represent back-trajectories arriving at 200, 500, and 1000 m AGL heights, respectively. Most of air masses were originated from Northern China near Nei Mongol desert and transported to the measurement site during the Asian dust periods. Since most of air masses were come from relatively cold and dry region in Northern China during Asian dust periods, relatively low RH of 54.0±19.4% was observed compared to that of 64.3±17.1% during the LTP periods. Air masses during the AD1_07 (27–28 March 2007), AD3_07 (8 May 2007), and AD4_07 (25–26 May 2007) periods were originated from Northern China and then transported across Eastern China. During the AD1_07 and AD3_07 periods, transports of anthropogenic aerosols from Eastern China were also clearly observed. Many hot spots of biomass burning in eastern coastal areas of China were observed during the

AD4_07 period. Therefore, relatively high $PM_{2.5}/PM_{10}$ mass ratio and $BC/PM_{10}$ ratio were observed during those periods. On the other hand, low $PM_{2.5}/PM_{10}$ mass ratio <~0.4 and $BC/PM_{10}$ ratio <~1.3 were measured during the AD2_07 (31 March–1 April 2007), AD5_07 (29 December 2007), AD1_08 (12 February 2008), and AD2_08 (16–17 March 2008) periods. During the Asian dust periods, Ångström exponent of aerosol extinction between 340–550 nm, $\alpha_e$(340–550 nm) was determined to be <0.40 except AD03_07 period. It was found that Asian dust event during spring frequently accompanies with anthropogenic pollutant emitted from industrial region of Eastern China.

Volume size distributions of ambient and volatile aerosols measured during the Asian dust periods are shown in Fig. 12. Contribution of volatile aerosol to ambient aerosol is also shown in the Figure. Elevated coarse mode volume distributions with peak values of ~200 $\mu m^3 cm^{-3}$ at 4–5 μm were observed during the Asian dust periods. Elevated concentrations observed in the fine mode during the AD3_07 and AD4_07 periods were mainly due to the influence of long-range transport anthropogenic aerosols from Asian continent. Elevated volume concentrations of volatile aerosol in fine region (diameter<2.5 μm) during the same periods are also clearly seen in the Fig. 12. After excluding the mixed cases (Asian dust plus LTP)-AD3_07 and AD4_07 periods, it was found that average contribution of volatile aerosol to ambient aerosol volume concentration was 14.7% and 6.5% in the fine and coarse mode, respectively, during the Asian dust period.

Aerosol $b_{scat}$ and $b_{abs}$ as well as SSA are plotted in Fig. 13a, b as a function of wavelength. Ångström exponents of SSA in the wavelength region of 370–520 nm ($\alpha_w$(370–520 nm)) and 590–950 nm ($\alpha_w$ (590–950 nm)) for each Asian dust period are also shown in Fig. 13c, d. Very low $b_{abs}$ of <10 $Mm^{-1}$ at 550 nm was observed during the AD5_07 and AD1_08 periods while it was in the range of 30–50 $Mm^{-1}$ during the remaining periods. Decreasing trend of $b_{abs}$ was observed during Asian dust periods as wavelength increases. On the other hand, $b_{scat}$ during the Asian dust periods was invariant with wavelength except for the AD1_07 and AD3_07 periods. Slightly decreasing trend of $b_{scat}$ observed during the AD1_07 and AD3_07 periods can be explained

by high spectral dependence of anthropogenic fine particles transported together with Asian dust particles. Based on the spectral characteristics of $b_{\text{scat}}$ and $b_{\text{abs}}$, spectral SSA during the Asian dust periods was determined and plotted in Fig. 13c, d. It is shown that SSA of Asian dust particles increases with wavelength. Higher spectral dependence of SSA was observed in the short wavelength region with $\alpha_{\text{w}}$ (370–520 nm) of $< -0.1$ except the AD5_07 period. Relatively low spectral dependence of SSA during the AD5_07 period was mainly due to very low fraction of BC to $PM_{10}$, ~0.4±0.3%. After excluding the mixed cases of AD1_07, AD3_07 and AD4_07, it was found that SSA of Asian dust aerosol was relatively high in the range of 0.92–0.97 at 550 nm with strong spectral dependence.

### 4.4.2 Long-range transport pollution aerosol

MODIS RGB images and Hysplit air mass back-trajectories arriving at the measurement site during LTP periods are shown in Fig. 14. Red, blue, and yellowish green lines represent back-trajectories arriving at 200, 500, and 1000 m AGL heights, respectively. During the LTP periods, most of air masses were originated from the industrial areas of Eastern China (Shanghai to Beijng regions) and transported to the measurement site. During the LTP02_07, LTP03_07, and LTP01_08 periods, MODIS RGB images clearly show the transport of anthropogenic aerosols from Eastern China to downwind areas. Spatial distributions of AOT over Northeast Asia during the LTP03_07 are shown in Fig. 15. On 22 October it is clearly seen that severe haze layer (AOT >1.0) lingered over Eastern China to Yellow Sea and then transported to Korean peninsula. Outflow of severe haze plume is also seen on 23 October. In this case, the haze plume emitted from Eastern China moved to south-east direction and then turned toward Korean peninsula, resulting in very high AOT over the measurement site on 24 October.

Observed aerosol physical and optical properties during the LTP periods are summarized in Table 5. Average $PM_{10}$ during the LTP periods ranged 75.7 µg m$^{-3}$ to 225.1 µg m$^{-3}$. Most severe LPT events were observed during 23–24 July 2007 (LTP01_07) and 6–8 January 2008 (LTP01_08) with average $PM_{10}$ concentrations of

176.9±40.7 and 152.0±24.6 $\mu$g m$^{-3}$, respectively. Since most of haze events were anthropogenic origin, high PM$_{2.5}$/PM$_{10}$ ratios of >0.87 was observed during the LTP periods except for the LTP04_07 period. Average BC/PM$_{10}$ and BC/PM$_{2.5}$ mass ratios were determined to be 5.7±2.0% (in the range of 3.6–7.4%) and 6.7±2.6% (4.4–9.2%),
5  respectively, during the LTP periods. The average of BC/PM$_{2.5}$ ratio in this study is comparable to 6.9% observed at an urban site in Beijing, China during the summer of 2006 (Jung et al., 2009a) and ∼7% at an urban site in Seoul, Korea during March 2003–February 2005, respectively (Kim et al., 2007). High values of $\alpha_e$ (340–550 nm) in the range of 0.85–1.20 were obtained with an average of 1.04 while $\alpha_e$ (550–1020 nm) was
10  in the range of 0.96–1.47 with an average of 1.35, which indicates dominance of small size particles in the LTP aerosols.

Aerosol volume size distributions of ambient and volatile aerosols measured during the LTP periods are shown in Fig. 16. Contributions of volatile aerosol to ambient aerosol are also shown in the Figure. Uni-modal distribution peaked at 4–5 $\mu$m was
15  observed during the Asian dust periods while tri-modal distributions with peak values at 0.4, 2, and 4–5 $\mu$m were observed during the LTP periods. Since LTP aerosols were anthropogenic origin, aerosol volume concentration peaked at 0.4 $\mu$m. Log volume distribution of volatile aerosols also shows a clear tri-modal distribution. Average contribution of volatile aerosol to ambient aerosol volume concentration was determined to
20  be 34.1% and 15.0% in the fine and coarse modes with the maximum value of 40–60% at 0.5–0.6 $\mu$m, which was almost 2.3 times higher than those obtained during the AD periods. This difference in volatility in the coarse mode of particles can be used as an indicator to classify the haze types such as LTP aerosol event and Asian dust events.

$b_{scat}$ and $b_{abs}$ as well as SSA during the LTP periods are shown in Fig. 17 as a func-
25  tion of wavelength. Average $b_{scat}$ and $b_{abs}$ during the LTP periods were measured to be 39.4–63.6 Mm$^{-1}$ and 485.8–1280.7 Mm$^{-1}$, respectively. Decreasing trend of $b_{scat}$ and $b_{abs}$ with wavelength was observed during the LTP periods. Due to these decreasing trend of $b_{scat}$ and $b_{abs}$ with wavelength, SSA showed little spectral dependence during the LTP periods except below 550 nm. Besides the LTP04_07 period of relatively

low SSA <0.89 at 550 nm, average SSA was determined to be 0.94–0.96 at 550 nm during the LTP periods. Ångström exponent of SSA in two wavelength ranges; $\alpha_w$ (370–520 nm) and $\alpha_w$ (590–950 nm) are also shown in Fig. 17. Low value of $\alpha_w$ was obtained compared to that of the Asian dust periods. This study suggests that it is possible to classify haze types based on the physical and optical properties of aerosol. Asian dust event can be classified as low $PM_{2.5}/PM_{10}$ mass ratio of $<\sim0.4$, $BC/PM_{10}$ ratio of $<\sim1.3\%$, and $\alpha_e$ (340–550 nm) of <0.40 as well as low contribution of volatile aerosol to ambient aerosol of <10%. However, LTP event can be classified as high $PM_{2.5}/PM_{10}$ mass ratio, $BC/PM_{10}$ ratio of >3.6%, and $\alpha_e$ (340–550 nm) of >0.85 as well as increased contribution of volatile aerosol to ambient aerosol.

## 5 Conclusions

Based on the aerosol optical and physical properties measured for one year at an urban site (37.57° N, 126.94° E) in Seoul, Korea, characteristics of aerosol spectral optical properties including single scattering albedo (SSA) have been investigated in this study. From the spectral dependence of $b_{scat}$ under relatively dry and humid conditions, increases of SSA and particle size were clearly observed through water uptake under humid condition-especially in summer. It was found that aerosol water content is one of important parameter to determine $b_{scat}$ and SSA as well as particle size during humid summer period. It was found that on average SSA decreased by 7% due to contribution by aerosol water content. Since mass fraction of sulfate and nitrate to total mass was dominantly increased during the pollution event periods in the Megacities of Korea (Kim et al., 2007) and China (Jung et al., 2009a,b), higher SSA during these periods was mainly due to the increased contribution of light scattering by secondary aerosols. From the calibration study between thermally measured EC and optically measured BC, clear seasonal variation of mass attenuation efficiency ($\sigma_{ATN}=b_{ATN}/EC$) was observed with the maximum value in summer. High $\sigma_{ATN}$ in summer can be attributed to the enhancement of light attenuation capacity of EC through the change of

its mixing state. Therefore, it is recommended that a proper seasonal $\sigma_{ATN}$ value be used for filter based BC measurement.

From MODIS satellite AOT and Hysplit air mass backward trajectory analyses as well as chemical analysis, it was found that Asian dust event occurred during spring frequently accompanies with anthropogenic pollutant emitted from industrial region of Eastern China. Increasing trend of SSA with wavelength was observed during the Asian dust period while little spectral dependence of SSA was observed except below 500 nm during long-range transport pollution (LTP) periods. Although there still exist large uncertainties in radiative transfer calculations for determining radiative forcing of atmospheric aerosol, few studies have been done regarding spectral optical properties of urban aerosol and Asian dust particle in Northeast Asia based on long-term continuous measurement data. Thus, aerosol spectral optical properties obtained in this study can provide useful information for quantifying aerosol's climate change effects.

# References

Andreae, M. O., Schmid, O., Yang, H., Chand, D., Yu, J. Z., Zeng, L., and Zhang, Y.: Optical properties and chemical composition of the atmospheric aerosol in urban Guangzhou, China Atmos. Environ., 42, 6335–6350, 2008.

Arnott, W. P., Hamasha, K., Moosmüller, H., Sheridan, P. J., and Ogren, J. A.: Towards aerosol light-absorption measurements with a 7-wavelength aethalometer: evaluation with a photoacoustic instrument and 3-wavelength nephelometer, Aerosol Sci. Tech., 39, 17–29, 2005.

Badarinath, K. V. S., Kharol, S. K., and Sharma, A. R.: Long-range transport of aerosols from agriculture crop residue burning in Indo-Gangetic Plains – A study using LIDAR, ground measurements and satellite data, J. Atmos. Sol.-Terr. Phy., 71, 112–120, 2009.

**Spectral aerosol optical properties**

J. Jung et al.

Ballach, J., Hitzenberger, R., Schultz, E., and Jaeschke, W.: Development of an improved optical transmission technique for black carbon (BC) analysis, Atmos. Environ., 35, 2089–2100, 2001.

Balis, D. S., Amiridis, V., Zerefos, C., Gerasopoulos, E., Andreae, M., Zanis, P., Kazantzidis, A., Kazadzi, S., and Papayannis, A.: Raman lidar and sunphotometric measurements of aerosol optical properties over Thessaloniki, Greece during a biomass burning episode, Atmos. Environ., 37(32), 4529–4538, 2003.

Bergin, M. H., Cass, G. R., Xu, J., Fang, C., Zeng, L. M., Yu, T., Salmon, L. G., Kiang, C. S., Tang, X. Y., Zhang, Y. H., and Chameides, W. L.: Aerosol radiative, physica, and chemical properties in Beijing during June 1999, J. Geophys. Res., 106(D16), 17969–17980, 2001.

Birch, M. E. and Cary, R. A.: Elemental carbon-based method for monitoring occupational exposures to particulate Diesel exhaust, Aerosol Sci. Tech., 25, 221–241, 1996.

Bond, T. C.: Spectral dependence of visible light absorption by carbonaceous particles emitted from coal combustion, Geophys. Res. Lett., 28, 4075–4078, 2001.

Draxler, R. R. and Rolph, G. D.: HYSPLIT (HYbrid Single-Particle Lagrangian Integrated Trajectory) Model access via NOAA ARL READY Website (http://www.arl.noaa.gov/HYSPLIT.php), NOAA Air Resources Laboratory, Silver Spring, MD, 2003.

Dubovik, O., Holben, B., Eck, T. F., Smirnov, A., Kaufman, Y. J., King, M. D., Tanre, D., and Slutsker, I.: Variability of absorption and optical properties of key aerosol types observed in worldwide locations, J. Atmos. Sci., 59, 590–608, 2002.

Forster, P., Ramaswamy, V., Artaxo, P., Berntsen, T., R. Betts, Fahey, D. W., Haywood, J., Lean, J., Lowe, D. C., Myhre, G., Nganga, J., Prinn, R., Raga, G., Schulz, M., and Van Dorland, R.: Changes in Atmospheric Constituents and in Radiative Forcing, in: Climate Change 2007: The Physical Science Basis. Contribution of Working Group I to the Fourth Assessment Report of the Intergovernmental Panel on Climate Change, edited by: Solomon, S., Qin, D., Manning, M., Chen, Z., Marquis, M., Averyt, K. B., Tignor, M., and Miller, H. L., Cambridge University Press, Cambridge, UK and New York, NY, USA, 2007.

Grimm, H.: Field experience of portable aerosol spectrometer for simultaneous monitoring of $PM_{10}$, $PM_{2.5}$ and $PM_{1.0}$, AAAR Conference, Atlanta, 2002.

Grim, H. and Eatough, D. J.: Aerosol measurement: the use of optical light scattering for the determination of particulate size distribution, and particulate mass, including the semi-volatile fraction, J. Air Waste Manage., 59, 101–107, 2009.

Hansen, A. D. A.: The Aethalometer, manual, Magee Scientific, Berkeley, California, USA,

2005.

Heintzenberg, J., Charlson, R. J., Clarke, A. D., Liousse, C., Ramaswamy, V., Shine, K. P., Wendisch, M., and Helas, G.: Measurements and modeling of aerosol single-scattering albedo: progress, problems and prospects, Atmos. Phys., 70, 249– 263, 1997.

Höller, R., Ito, K., Tohno, S., and Kasahara, M.: Wavelength-dependent aerosol single-scattering albedo: measurements and model calculations for a coastal site near the Sea of Japan during ACE-Asia, J. Geophys. Res., 108(D23), 8648, doi:10.1029/2002JD003250, 2003.

Jacob, D. J., Logan, J. A., and Murti, P. P.: Effect of rising Asian emissions on surface ozone in the United States, Geophys. Res. Lett., 26, 2175–2178, 1999.

Jacobson, M. Z.: Strong radiative heating due to the mixing state of black carbon in atmospheric aerosols, Nature, 409(6821), 672–695, 2001.

Jeong, C.-H., Hopke, P. K., Kim, E., and Lee, D.-W.: The comparison between thermal-optical transmittance elemental carbon and Aethalometer black carbon measured at multiple monitoring sites, Atmos. Environ., 38, 5193–5204, 2004.

Jung, J. S., Lee, H. L., Kim, Y. J., Liu, X., Liu, X., Zhang, Y., Hu, M., and Sugimoto, M.: Optical properties of atmospheric aerosols obtained by in-situ and remote measurements during 2006 CAREBEIJING campaign, J. Geophys. Res., 114, D00G02, doi:10.1029/2008JD010337, 2009a.

Jung, J. S., Lee, H. L., Kim, Y. J., Liu, X., Zhang, Y., Gu, J., and Fan, S.: Aerosol chemistry and the effect of aerosol water content on visibility impairment and radiative forcing in Guangzhou during the 2006 Pearl River Delta campaign, J. Environ. Manage., 90, 3231–3244, 2009b.

Kim, H.-S., Huh, J.-B., Hopke, P. K., Holsen, T. M., and Yi, S.-M.: Characteristics of the major chemical constituents of $PM_{2.5}$ and smog events in Seoul, Korea in 2003 and 2004, Atmos. Environ., 41, 6762–6770, 2007.

Kim, K. W., Kim, Y. J., and Oh, S. J.: Visibility impairment during yellow sand periods in the urban atmosphere of Kwangju, Korea, Atmos. Environ., 35, 5157–5167, 2001.

Kim, Y. J., Kim, M. J., Lee, K. H., and Park, S. S.: Investigation of carbon pollution episodes using semi-continuous instrument in Incheon, Korea, Atmos. Environ., 40(22), 4064–4075, 2006.

Kim, J. Y.: Transport routes and source regions of Asian dust observed in Korea during the past 40 years (1965–2004), Atmos. Environ., 42, 4778–4789, 2008.

Kondo, Y., Sahu, L., Kuwata, M., Miyazaki, Y., Takegawa, N., Moteki, N., Imaru, J., Han, S.,

Nakayama, T., Kim Oanh, N. T., Min, H., Kim, Y. J., and Kita, K.: Stabilization of the mass absorption cross section of black carbon for filter-based absorption photometry by the use of a heated inlet, Aerosol Sci. Tech., 43(8), 741–756, 2009.

Kopp, C., Petzold, A., and Niessner, R.: Investigation of the specific attenuation cross-section of aerosols deposited on fiber filters with a polar photometer to determine black carbon, J. Aerosol Sci., 30, 1153–1163, 1999.

Lee, K. H., Kim, J. E., Kim, Y. J., Kim, J., and von Hoyningen-Huene, W.: Impact of the smoke aerosol from Russian forest fires on the atmospheric environment over Korea during May 2003, Atmos. Environ., 39(1), 85–99, 2005.

Lee, K. H., Kim, Y. J., von Hoyningen-Huene, W., and Burrow, J. P.: Spatio-temporal variability of satellite-derived aerosol optical thickness over Northeast Asia in 2004, Atmos. Environ., 41, 3959–3973, 2007.

Levy, R. C., Remer, L. A., and Dubovik, O.: Global aerosol optical properties and application 15 to moderate resolution imaging spectroradiometer aerosol retrieval over land, J. Geophys. Res., 112(D13), D13210, doi:10.1029/2006JD007815, 2007a.

Levy, R. C., Remer, L. A., Mattoo, S., Vermote, E. F., and Kaufman, Y. J.: Second-generation operational algorithm: retrieval of aerosol properties over land from inversion of moderate resolution imaging spectroradiometer spectral reflectance, J. Geophys. Res., 112(D13), D13211, doi:10.1029/2006JD007811, 2007b.

Li, C., Marufu, L. T., Dickerson, R. R., Li, Z., Wen, T., Wang, Y., Wang, P., Chen, H., and Stehr, J. W.: In situ measurements of trace gases and aerosol optical properties at a rural site in Northern China during east asian study of tropospheric aerosols: an international regional experiment 2005, J. Geophys. Res., 112, D22S04, doi:10.1029/2006JD007592, 2007.

Nakajima, T., Tonna, G., Rao, R., Boi, P., Kaufman, Y., and Holben, B.: Use of sky brightness measurements from ground for remote sensing of particulate poly dispersions, Appl. Optics, 35(15), 2672–2686, 1996.

OPTEC: Model NGN-2 Open-Air Integrating Nepheolometer: Technical Manual for Theory of Operation and Operating Procedures, OPTEC Inc., 199 Smith Street Lowell, MI 49331, USA, 1993.

Park, S. S., Kim, Y. J., and Kang, C. H.: Atmospheric polycyclic aromatic hydrocarbons in Seoul, Korea, Atmos. Environ., 36, 2917–2924, 2002.

Park, S. U. and Kim, J. W.: Aerosol size distributions observed at the Seoul National University campus in Korea during the Asian dust and non-Asian dust periods, Atmos. Environ., 40,

**Spectral aerosol optical properties**

J. Jung et al.

1722–1730, 2006.

Petzold, A., Kopp, C., and Niessner, R.: The dependence of the specific attenuation cross section on black carbon mass fraction and particle size, Atmos. Environ., 31, 661–672, 1997.

Polidori, A., Turpin, B. J., Lim, H.-J., Cabada, J. C., Subramanian, R., Pandis, S. N., and Robinson, A. L.: Local and regional secondary organic aerosol: insights from a year of semi-continuous carbon measurements at Pittsburgh, Aerosol Sci. Tech., 40, 861–872, 2006.

Ramaswamy, V., Boucher, O., Haigh, J., et al.: Radiative forcing of climate change, in: Climate Change 2001: The Scientific Basis. Contribution of Working Group I to the Third Assessment Report of the Intergovernmental Panel on Climate Change, edited by: Houghton, J. T., Ding, Y., Griggs, D. J., et al., Cambridge University Press, Cambridge, UK and New York, NY, USA, 349–416, 2001.

Rolph, G. D.: Real-time Environmental Applications and Display sYstem (READY), Website (http://www.arl.noaa.gov/ready.php), NOAA Air Resources Laboratory, Silver Spring, MD, 2003.

Ryu, S. Y., Kwon, B. G., Kim, Y. J., Kim, H. H., and Chun, K. J.: Characteristics of biomass burning aerosol and its impact on regional air quality in the summer of 2003 at Gwangju, Korea, Atmos. Res., 86, 362–373, 2006.

Schmid, O., Artaxo, P., Arnott, W. P., Chand, D., Gatti, L. V., Frank, G. P., Hoffer, A., Schnaiter, M., and Andreae, M. O.: Spectral light absorption by ambient aerosols influenced by biomass burning in the Amazon Basin. I: Comparison and field calibration of absorption measurement techniques, Atmos. Chem. Phys., 6, 3443–3462, 2006, http://www.atmos-chem-phys.net/6/3443/2006/.

Snyder, D. C. and Schauer, J. J.: An inter-comparison of two black carbon aerosol instruments and a semi-continuous elemental carbon instrument in the urban environment, Aerosol Sci. Tech., 41, 463–474, 2007.

Stohl, A.: Computation, accuracy and applications of trajectories. A review and bibliography, Atmos. Environ., 32(6), 947–966, 1998.

Turpin, B. J., Saxena, P., and Andrews, E.: Measuring and simulating particulate organics in the atmosphere: problems and prospects, Atmos. Environ., 34, 2983–3013, 2000.

Weingartner, E., Saathoff, H., Schnaiter, M., Streit, N., Bitnar, B., and Baltensperger, U.: Absorption of light by soot particles: determination of the absorption coefficient by means of aethalometers, J. Aerosol Sci., 34, 1445–1463, 2003.

**Table 1.** Measurement parameters and instrument conditions used in this study.

| Measurement parameters | Instrument | Particle size range | Time interval |
|---|---|---|---|
| Organic carbon/elemental carbon (OC/EC) | Semi-continuous OC/EC analyzer (Sunset Lab., RT3015) | $D_p < 2.5\,\mu m$ | 1 h |
| Black carbon (BC) | 7-$\lambda$ Aethalometer (Magee Scientific, AE31) | $D_p < 2.5\,\mu m$ | 5 min |
| Light scattering coefficient ($b_{scat}$) | Nephelometer (Optec, NGN-2) | $D_p > 0\,\mu m$ | 2 min |
| Aerosol optical thickness (AOT) | Skyradiometer (PREDE, POM-2) | $D_p > 0\,\mu m$ | 10 min |
| PM$_{10}$, PM$_{2.5}$, PM$_{1.0}$ Ambient/ Volatile mass concentrations | Aerosol Spectrometer (Grimm, 265) | $D_p < 10\,\mu m$, 2.5 µm, 1.0 µm | 30 min |
| PM size distribution | | $D_p > 0.25\,\mu m$ | 1 min |

**Table 2.** Detection limit and uncertainties of the measurement parameters.

| Instrument | Parameter | Unit | Dynamic blank | Standard deviation ($\sigma$) | Detection limit ($3\sigma$) | Uncertainty (%) |
|---|---|---|---|---|---|---|
| Aethalometer (Magee, AE31) | BC (370 nm) | $\mu g\,m^{-3}$ | 0.105 | 0.052 | 0.156 | |
| | BC (470 nm) | | 0.115 | 0.054 | 0.161 | |
| | BC (520 nm) | | 0.106 | 0.062 | 0.187 | |
| | BC (590 nm) | | 0.111 | 0.071 | 0.213 | 10% |
| | BC (660 nm) | | 0.096 | 0.076 | 0.228 | |
| | BC (880 nm) | | 0.090 | 0.088 | 0.263 | |
| | BC (950 nm) | | 0.097 | 0.094 | 0.281 | |
| Sunset OC/EC analyzer (Sunset, RT3015) | OC | $\mu g\,C$ | 0.317 | 0.129 | 0.386 | |
| | EC | | 0.001 | 0.003 | 0.009 | 5% |
| | Opt.EC | | 0.017 | 0.008 | 0.024 | |
| Nephelometer (Optec, NGN2) | $b_{scat}$ | $Mm^{-1}$ | 0.554 | 1.441 | 4.321 | 10% |
| Aerosol Spectrometer (Grimm, 265) | $PM_{10}/PM_{2.5}/PM_{1.0}$ | $\mu g\,m^{-3}$ | | | 1.0 | 2%[1] |

[1] Reproducibility of the aerosol spectrometer in particle counting.

**Table 3.** Multiple scattering correction factor used for aethalometer measurement.

| Aerosol type | $C^*$ | Reference |
|---|---|---|
| Pure or external mixture of soot | 1.8–2.2 | Arnott et al. (2005) at $\lambda=521$ nm |
| Urban (internally mixture) | 3.7 | |
| Pure or external mixture of soot | 2.14 | Weingartner et al. (2003) at $\lambda=532$ nm |
| Soot coated with organic carbon (internally mixture) | 3.6 | |
| Ambient aerosol (internally mixture) | 4.55 | Schmid et al. (2006), at $\lambda=532$ nm |
| Pure or external mixture of soot | **2.1** | Suggested by Schmid et al. (2006) at $\lambda=532$ nm |
| Internally mixture of soot | **4.0** | |

**Table 4.** Summary of aerosol physical and optical properties measured during different Asian dust periods.

| Category | Period | $PM_{10}$ ($\mu g\,m^{-3}$) | $PM_{2.5}$ ($\mu g\,m^{-3}$) | $PM_{2.5}/PM_{10}$ (%) | $BC/PM_{10}$ (%) | RH (%) | $\alpha_e$ (340–550 nm) | $\alpha_e$ (550–1020 nm) |
|---|---|---|---|---|---|---|---|---|
| AD1_07 | 27–28 Mar 2007 | 253.8±45.0 | 86.9±28.0 | 36.5 | 2.8±1.2 | 69.2±7.6 | 0.39 | 0.44 |
| AD2_07 | 31 Mar–1 Apr 2007 | 544.1±250.6 | 74.9±34.0 | 14.3 | 0.9±0.3 | 60.5±19.0 | 0.13 | 0.11 |
| AD3_07 | 8 May 2007 | 173.7±51.1 | 108.4±7.9 | 66.2 | 3.7±0.8 | 49.4±7.1 | 0.56 | 0.47 |
| AD4_07 | 25–26 May 2007 | 252.2±59.2 | 154.6±48.1 | 60.2 | 2.1±0.6 | 64.4±16.5 | 0.18 | 0.17 |
| AD5_07 | 29 Dec 2007 | 303.6±77.0 | 104.4±11.2 | 35.8 | 0.4±0.3 | 52.9±13.7 | 0.03 | 0.03 |
| AD1_08 | 12 Feb 2008 | 123.8±18.6 | 33.4±5.4 | 27.2 | 0.8±0.3 | 23.6±4.5 | 0.36 | 0.36 |
| AD2_08 | 16–17 Mar 2008 | 149.6±13.2 | 48.5±4.0 | 32.5 | 1.3±0.4 | 43.2±16.1 | NA | NA |

**Table 5.** Summary of aerosol physical and optical properties measured during different long-range transport pollution (LTP) periods.

| Category | Period | $PM_{10}$ ($\mu g\,m^{-3}$) | $PM_{2.5}$ ($\mu g\,m^{-3}$) | $PM_{2.5}/PM_{10}$ (%) | $BC/PM_{10}$ (%) | RH (%) | $\alpha_e$ (340–550 nm) | $\alpha_e$ (550–1020 nm) |
|---|---|---|---|---|---|---|---|---|
| LTP01_07 | 23–24 Jul 2007 | 176.9±40.7 | 163.7±40.9 | 92.1 | 4.0±1.0 | 70.2±15.5 | 0.99 | 1.38 |
| LTP02_07 | 10–13 Sep 2007 | 125.4±27.2 | 108.9±25.4 | 86.7 | 6.1±1.4 | 72.2±11.8 | 1.20 | 1.47 |
| LTP03_07 | 23–25 Oct 2007 | 128.6±22.7 | 112.3±20.9 | 87.2 | 6.1±1.3 | 71.7±14.9 | 1.05 | 1.45 |
| LTP04_07 | 6–9 Nov 2007 | 115.9±20.8 | 94.9±18.7 | 81.7 | 7.4±2.8 | 54.3±15.4 | 1.16 | 1.43 |
| LTP01_08 | 6–8 Feb 2008 | 152.0±24.6 | 136.6±24.4 | 89.7 | 6.5±1.5 | 77.7±10.2 | 0.85 | 0.96 |
| LTP02_08 | 11–13 Mar 2008 | 122.4±11.3 | 111.0±10.4 | 90.7 | 5.0±0.7 | 54.9±12.6 | 1.00 | 1.40 |
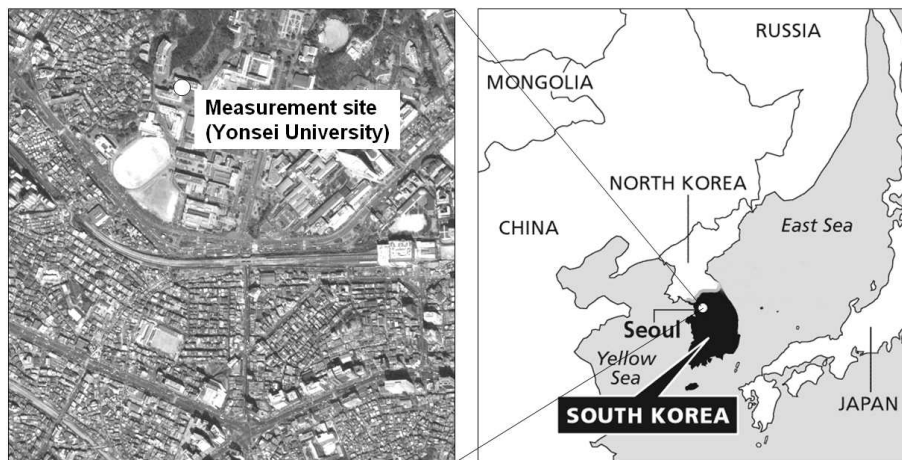
**Fig. 1.** Area map of the measurement site in Seoul, Korea.
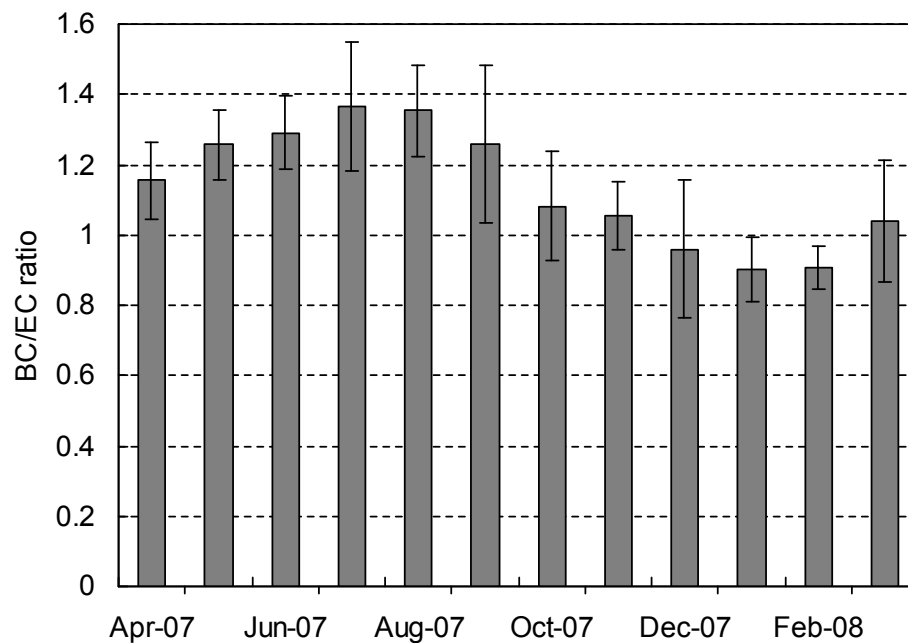
**Fig. 2.** Temporal variations of BC/EC ratio.
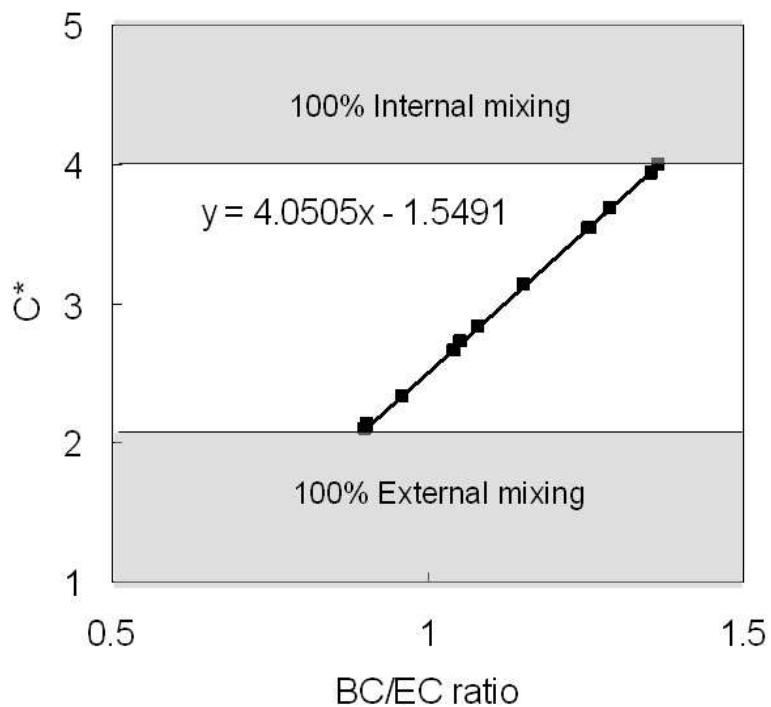
**Fig. 3.** Retrieval of multiple scattering correction factor for aethalometer measurement.
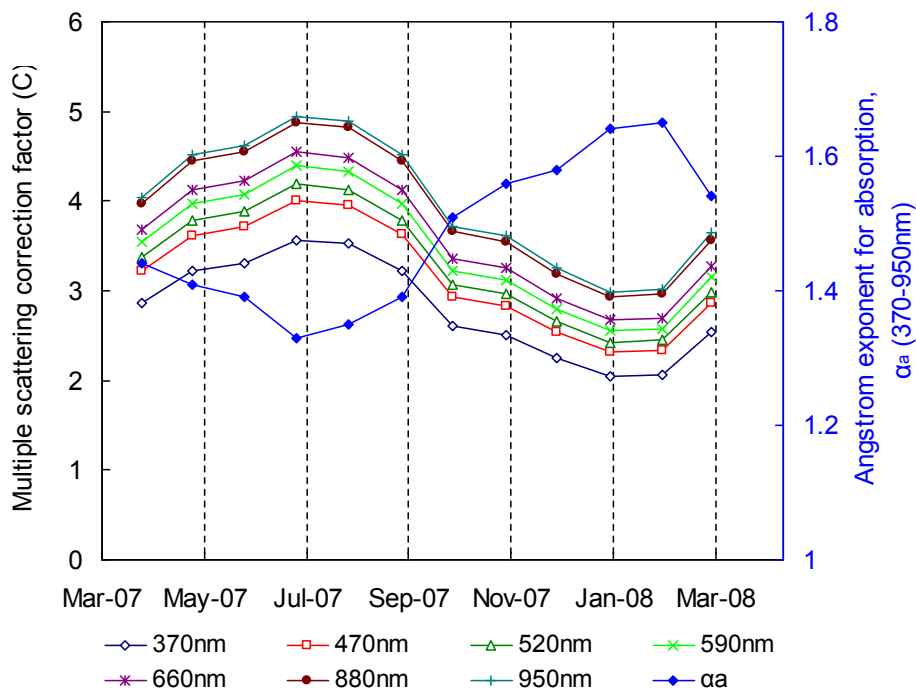
**Fig. 4.** Determination of the Ångström exponent for absorption ($\alpha_a$) in the range of 370 nm–950 nm and multiple scattering correction factor ($C$) at the measurement site.
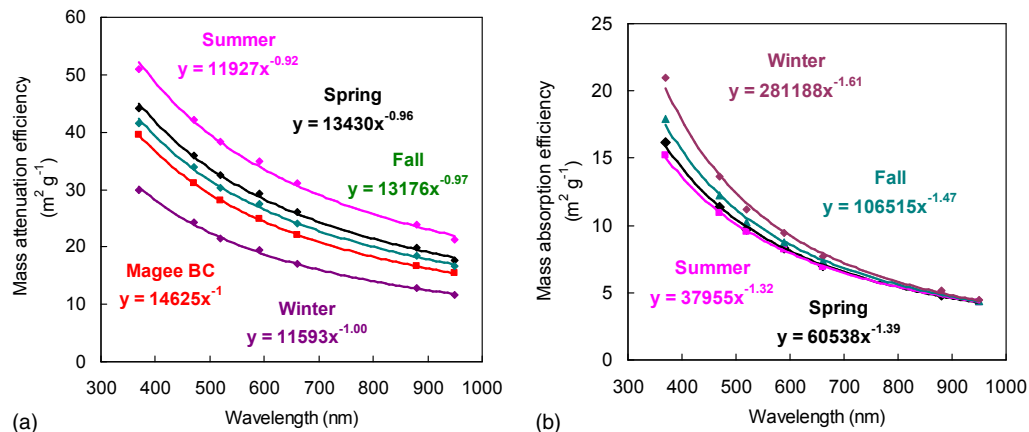
**Fig. 5.** Seasonal variations of specific attenuation efficiency of Aethalometer BC **(a)** and mass absorption efficiency of EC **(b)** as a function of wavelength.

**ACPD**

10, 2397–2444, 2010

**Spectral aerosol optical properties**

J. Jung et al.

Title Page

Abstract | Introduction

Conclusions | References

Tables | Figures

◄ | ►

◄ | ►

Back | Close

Full Screen / Esc

Printer-friendly Version

Interactive Discussion
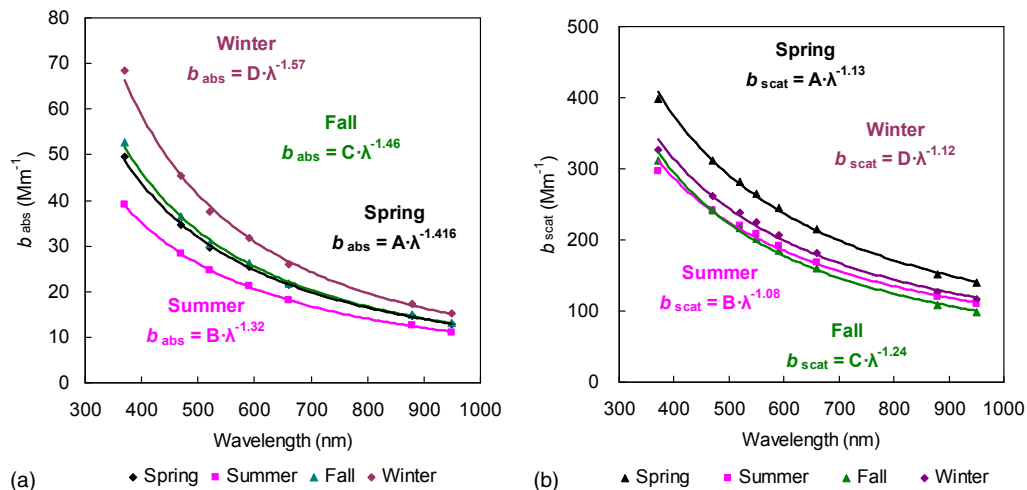
**Fig. 6.** Seasonal variations of light absorption ($b_{abs}$) **(a)** and light scattering coefficient ($b_{scat}$) **(b)** as a function of wavelength.
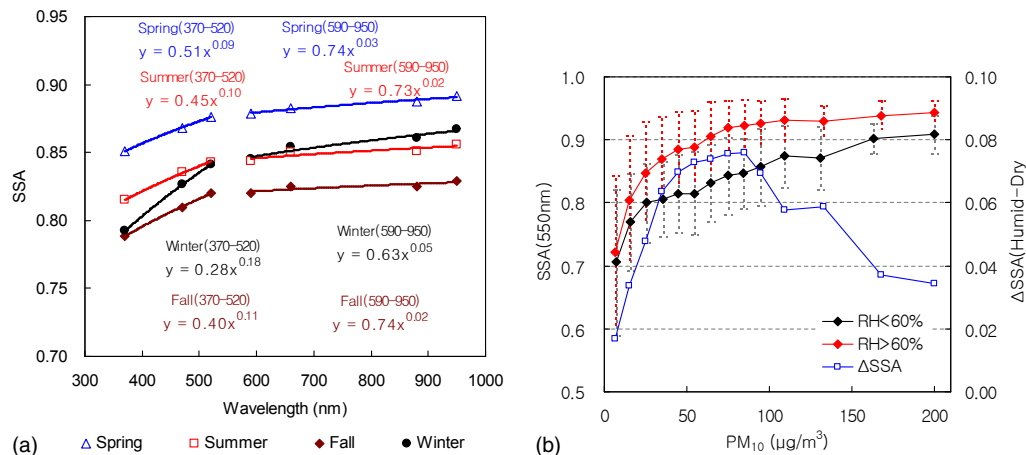
**Fig. 7.** Seasonal variations of aerosol single scattering albedo (SSA) as a function of wavelength **(a)** and SSA at 550 nm wavelength as a function of $PM_{10}$ mass concentration under relatively dry (RH<60%) and humid (RH>60%) conditions, respectively **(b)**.
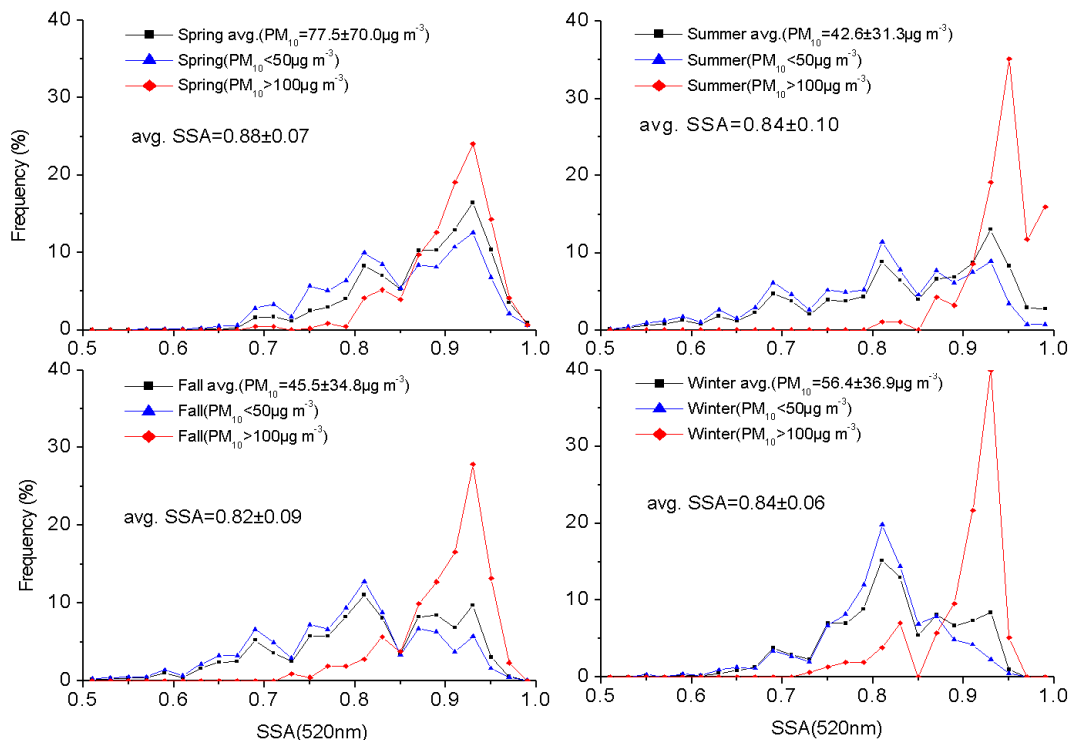
**Fig. 8.** Frequency distributions of aerosol single scattering albedo (SSA) at 550 nm during spring, summer, fall, and winter, respectively. Blue triangle and red diamond represent relatively clean ($PM_{10} < 50\,\mu g\,m^{-3}$) and polluted ($PM_{10} > 100\,\mu g\,m^{-3}$) periods, respectively.
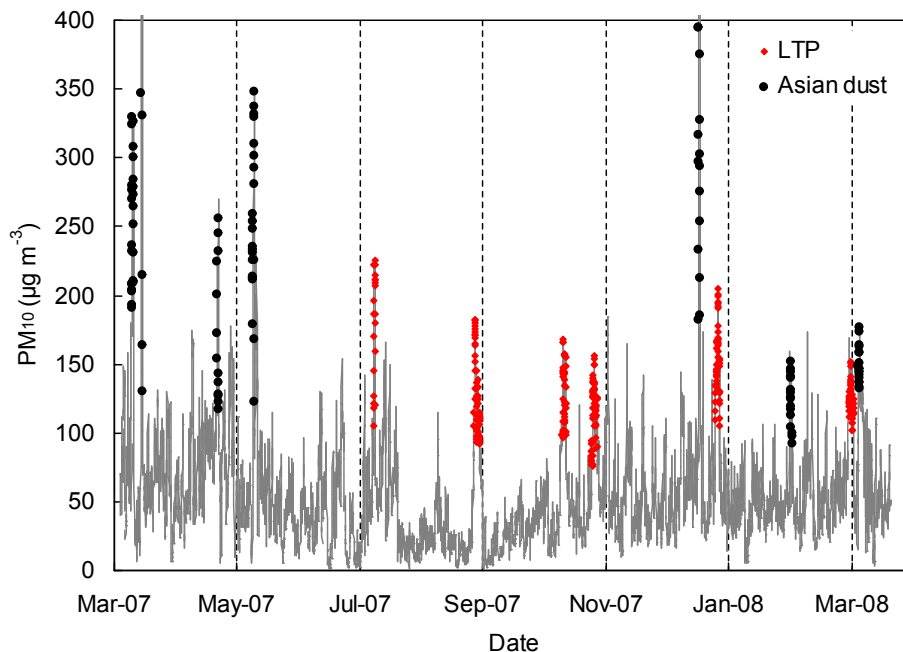
**Fig. 9.** Temporal variation of PM$_{10}$ mass concentration in Seoul, Korea during the entire measurement period. Red and black circles represent long-range transport pollution (LTP) and Asian dust periods, respectively.
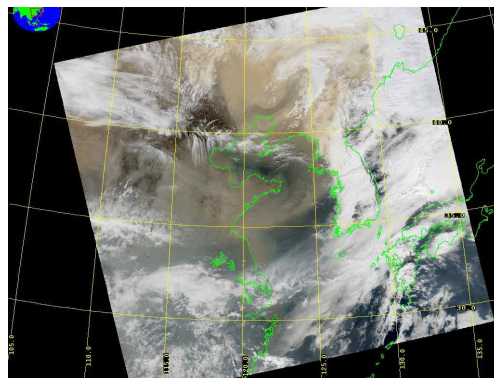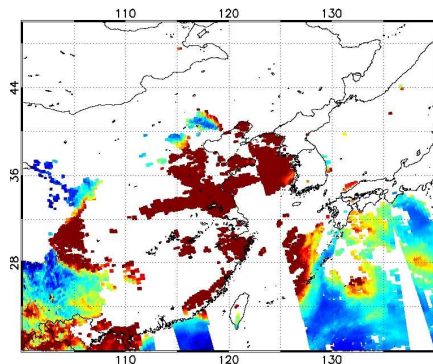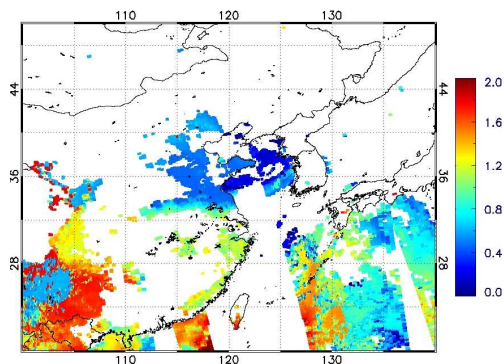
**Fig. 10.** MODIS RGB image **(a)**, aerosol optical thickness (AOT) **(b)**, and AOT Ångström exponent **(c)** during an Asian dust event on 31 March 2007.
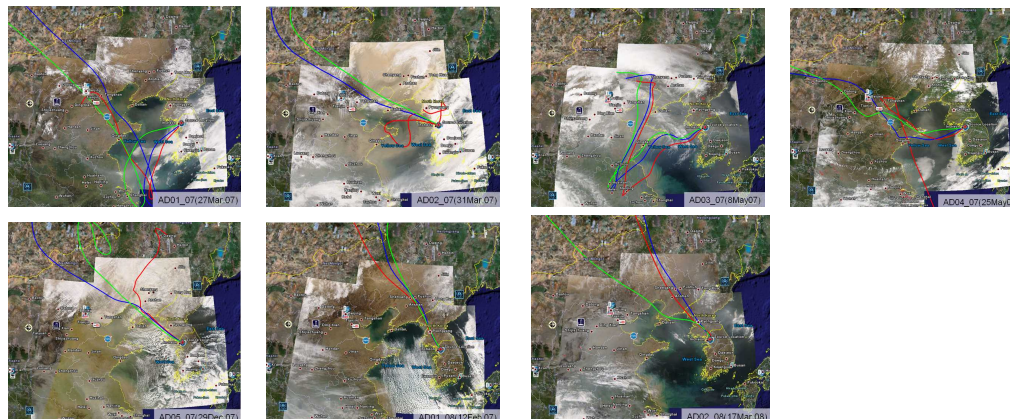
**Fig. 11.** MODIS RGB images and back-trajectories during the Asian dust periods arriving at the measurement site. Red, blue, and yellowish green are back-trajectories arriving 200, 500, and 1000 m altitudes, respectively.
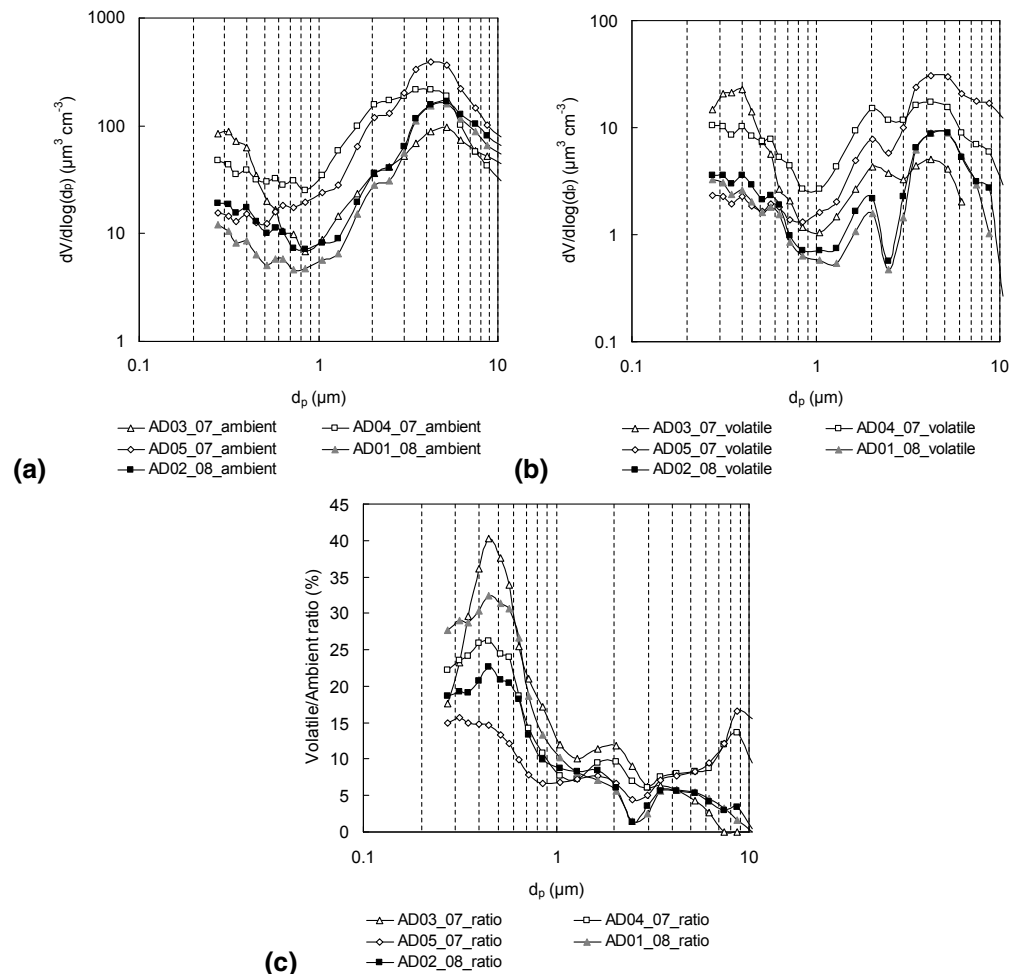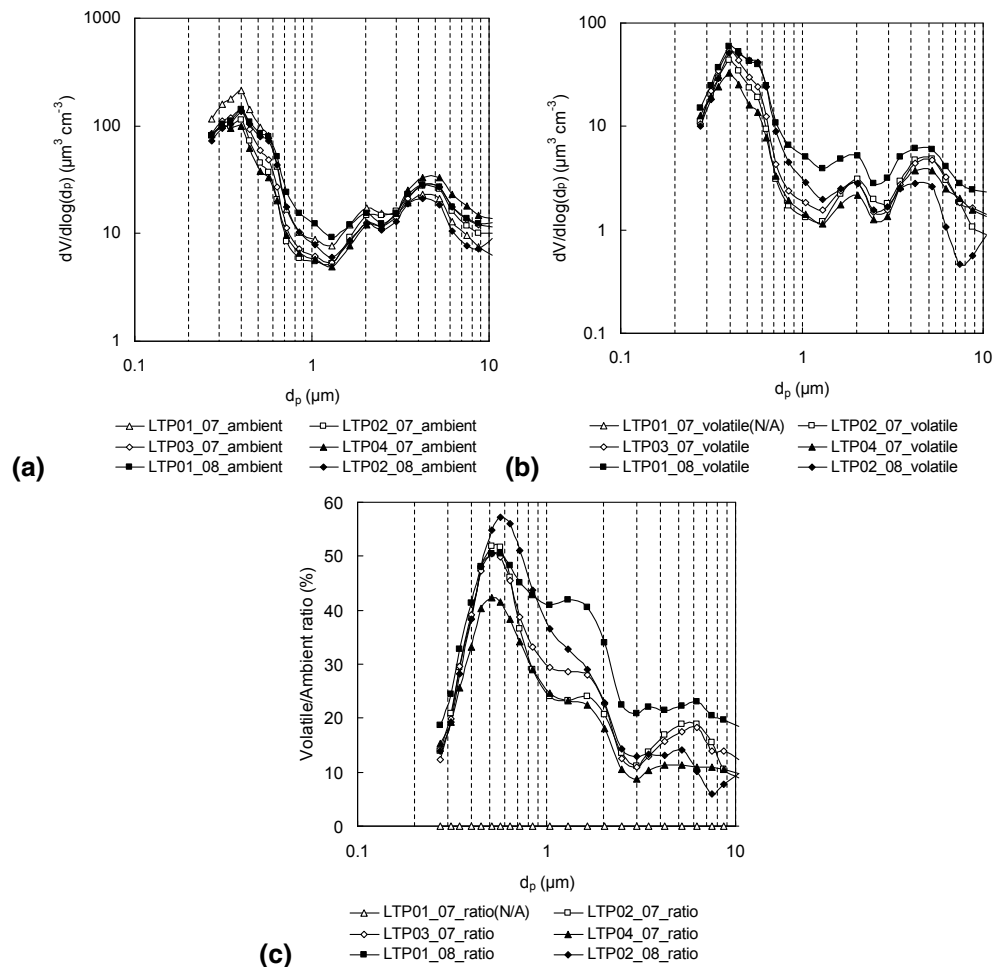
**Fig. 12.** Volume size distribution of ambient **(a)**, volatile aerosol **(b)**, and contribution of volatile fraction to ambient aerosol **(c)** during the Asian dust periods.
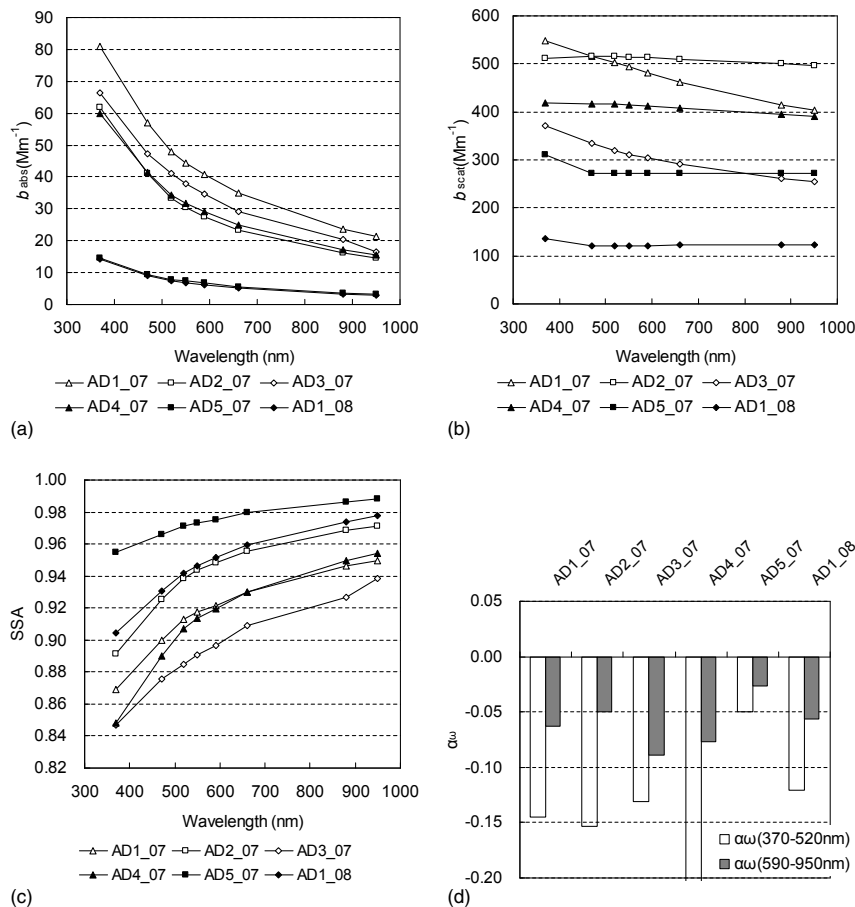
**Fig. 13.** Aerosol light scattering ($b_{scat}$) **(a)**, absorption coefficient ($b_{abs}$) **(b)**, and aerosol single scattering albedo (SSA) as a function of wavelength **(c)** as well as Ångström exponent ($\alpha_{\omega}$) of SSA **(d)** during the Asian dust periods.
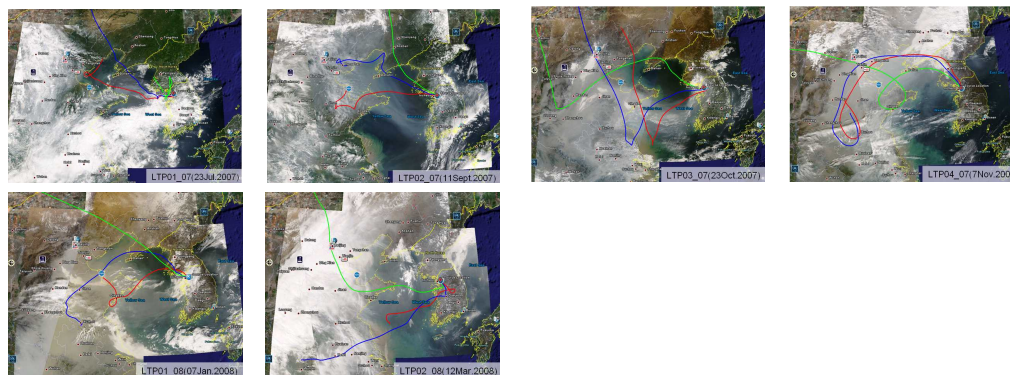
**Fig. 14.** MODIS RGB images and back-trajectories during the long-range transport pollution (LTP) periods. Red, blue, and yellowish green are back-trajectories arriving 200, 500, and 1000 m altitudes, respectively.
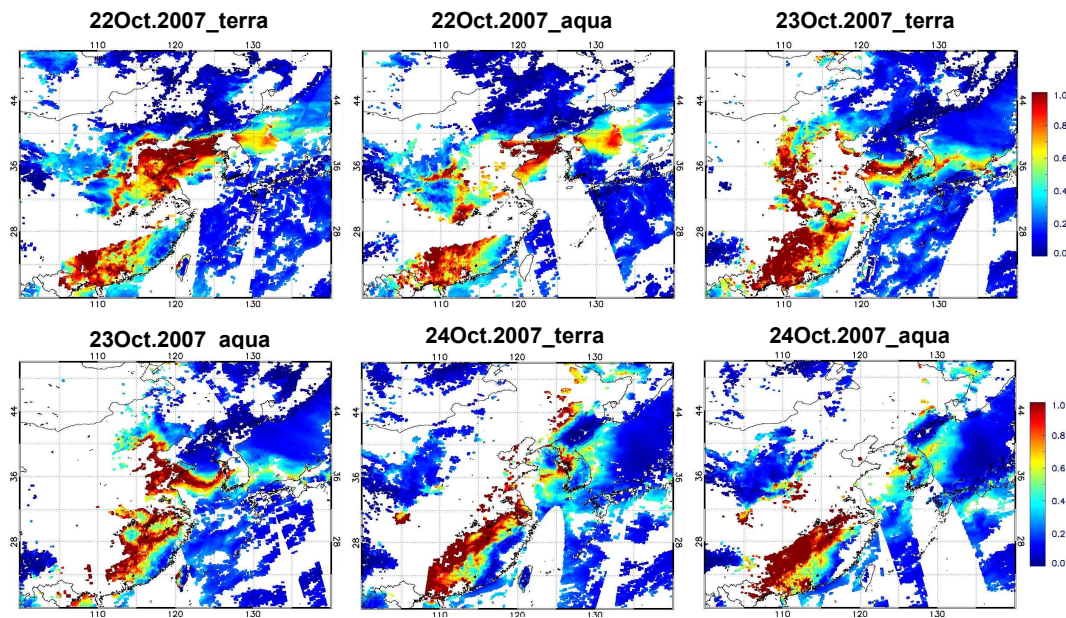
**Fig. 15.** Spatial distribution of aerosol optical thickness (AOT) over Northeast Asia during selected days of LRT period.

**Fig. 16.** Volume size distribution of ambient **(a)**, volatile aerosol **(b)**, and contribution of volatile fraction to ambient aerosol **(c)** during the long-range transport pollution (LTP) periods.
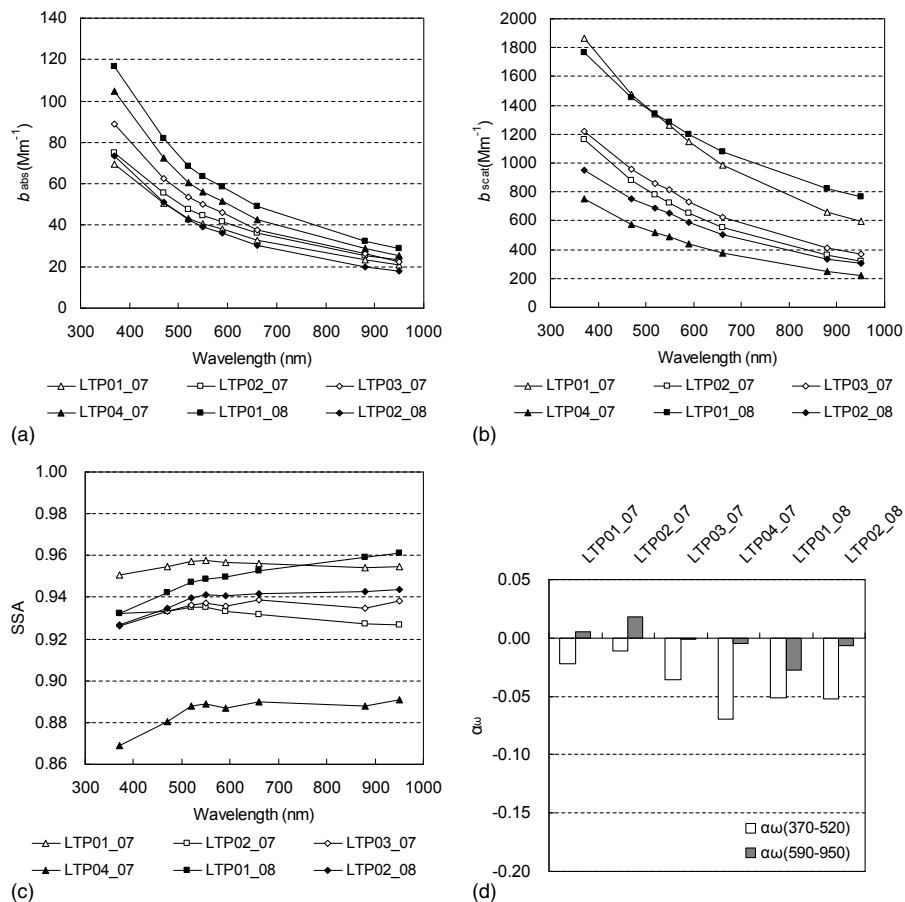
**Fig. 17.** Aerosol light scattering ($b_{scat}$) **(a)**, absorption coefficient ($b_{abs}$) **(b)**, and aerosol single scattering albedo (SSA) as a function of wavelength **(c)** as well as Ångström exponent ($\alpha_\omega$) of SSA **(d)** during the long-range transport pollution (LTP) periods.